Impact of Thermal Variations and Soldering Process on Performance and Behavior of MEMS Capacitive Accelerometers

Javier Martínez Lahoz, David Asiaín Ansorena, and José Ramón Beltrán Blázquez

***Abstract*—This work presents an analysis of performance and multiple parameters of microelectromechanical system (MEMS) capacitive accelerometers in applications with large thermal variations and the effects of the soldering process on them. The proposed test consists of a thermal characterization phase performed between two mechanical calibrations. The test is performed on multiple units before and after the soldering process. Mechanical, thermal, and performance parameters are analyzed and compared among all tests. The ranges and relative variations of these characteristics, both during the soldering process and the tests, have been identified and characterized individually. Mechanical bias shows greater variability than other parameters in both the soldering process and thermal tests. On the contrary, the thermal characteristic parameters show great stability in all cases. The thermal drifts, which are the main source of error in environments with large thermal variations, are successfully compensated for using a model with only two characteristic parameters. According to the observed behaviors, negative thermal variations (toward cooler temperatures) might be more suitable for thermal calibration due to other effects, such as creep, taking place primarily at hotter temperatures. The creep effect at constant temperature is analyzed according to the Kelvin–Voigt model with promising results, and a possible link between thermal drift and creep effects is presented. Performance results are calculated in multiple compensation scenarios. Using the proposed compensation techniques, the average maximum error is reduced from over 70 to 7 mg and the uncertainty is also reduced to a third of the initial value.**

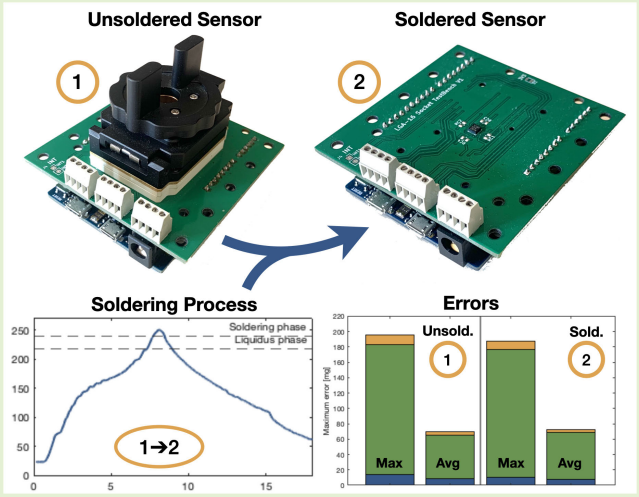

***Index Terms*—Creep, microelectromechanical system (MEMS), performance, soldering process, thermal drift, uncertainty.**

I. Introduction

MICROELECTROMECHANICAL sensors are increasingly becoming the main option as measurement tools in multiple fields, both in the scientific and consumer electronics scopes. The microelectromechanical system (MEMS) capacitive accelerometers have rapidly grown in popularity due to its advantages over traditional technologies such as low cost, small size, and low energy consumption [1], [2].

Manuscript received 4 September 2023; accepted 24 September 2023. Date of publication 6 October 2023; date of current version 14 November 2023. The associate editor coordinating the review of this article and approving it for publication was Prof. Mohsen Asadnia. *(Corresponding author: Javier Martínez Lahoz.)*

Javier Martínez Lahoz and David Asiaín Ansorena are with the Department of Electronic Engineering, Escuela Universitaria Politécnica de La Almunia, 50100 Zaragoza, Spain (e-mail: jmartinezlahoz@unizar.es; dasiain@unizar.es).

José Ramón Beltrán Blázquez is with the Department of Electronic Engineering and Communications, Universidad de Zaragoza, 50018 Zaragoza, Spain (e-mail: jrbelbla@unizar.es).

Digital Object Identifier 10.1109/JSEN.2023.3321238

Despite their advantages and widespread use, MEMS capacitive accelerometers also have some drawbacks in terms of accuracy and uncertainty that need to be addressed to achieve the best results. Among these drawbacks, thermal sensitivity has been widely studied. Thermal variations produce drifts in the data output that reduce the sensors reliability and need to be compensated in real applications [3], [4].

Other effects that can reduce the reliability of MEMS capacitive accelerometers are mechanical bias and sensitivity drifts, which can generate long-term drifts or poor performance. Stabilization of these effects can take up to six months if stored at room temperature [5]; however, these effects are accelerated with high temperatures. Many factors contribute to these long-term drifts, such as manufacturing imperfections, structural creep, and packaging techniques [6], [7], [8], [9].

Manufacturers of MEMS sensors usually state that due to the thermal sensitivity of these sensors, they should be soldered by taking into account some restrictions; mostly

related to the peak temperature and temperature gradients, both in the heating and cooling phases [10], [11], [12].

The aim of this work is to analyze the mechanical and thermal behavior of MEMS capacitive accelerometers in applications with large thermal variations and to study the effects of the soldering process on the performance of the sensor. A better understanding of this behavior could lead to more specific research and improvements in the performance of this technology.

This work presents a theoretical overview of the MEMS capacitive accelerometer and its application considerations in Section II; the proposed methodology and equipment used during the tests is described in Section III; Section IV describes the analysis performed on the data; Section V shows the results of the proposed tests; Section VI analyses the performance of the units during the tests and compares it with other studies; finally, in Section VII, the relevant information on the application of this technology is presented in a cohesive manner.

II. MEMS Accelerometer/Theoretical Analysis

A. Operating Principle

MEMS capacitive accelerometers are based on a spring-mass system, detecting external forces or accelerations according to the mass displacements. Although multiple sensing techniques can be used, all of them rely on one or multiple pairs of electrodes that form capacitor plates to measure the displacement. One of these plates is attached to the mass, or is part of the mass itself, and the other is fixed to the structure. External acceleration can be measured by detecting the change in capacitance between pairs of capacitor plates [13].

These sensing structures are manufactured on silicon, which is a temperature-sensitive material. Therefore, thermal variations can induce displacements of the mass due to asymmetric thermal expansion of beams, caused by manufacturing imperfections [14]. To improve the performance of these sensors and reduce thermal drifts, multiple works have been aimed at developing alternative design and sensing techniques for MEMS inertial units [15], [16].

B. Mechanical Calibration

Ideal triaxial accelerometers would have their three axes in a perfectly orthogonal arrangement. In reality, these sensors have cross-sensitivities among axes on top of sensitivity and bias errors. All three errors can be addressed with a mechanical calibration, obtaining the bias vector, B; the sensitivity matrix, S; and the cross-sensitivity matrix, A. The real acceleration, X_0, can be calculated from the measured acceleration X, using the aforementioned parameters according to the following equation [17], [18]:

$$X_0 = S \cdot A \cdot X + B. \tag{1}$$

Expanding this expression to its individual parameters and combining the sensitivity, cross-sensitivities parameters, and biases in a single matrix, the full calibration matrix, M, can be represented as in the following equation:

$$\begin{bmatrix} X_0 \\ Y_0 \\ Z_0 \end{bmatrix} = \begin{bmatrix} S_x & A_{yx} & A_{zx} & B_x \\ A_{xy} & S_y & A_{zy} & B_y \\ A_{xz} & A_{yz} & S_z & B_z \end{bmatrix} \cdot \begin{bmatrix} X \\ Y \\ Z \\ 1 \end{bmatrix} \tag{2}$$

where X_0, Y_0, and Z_0 are the axes raw measurements; X, Y, and Z are the real accelerations on the orthogonal axis; S_x, S_y, and S_z are the sensitivities of the axes; B_x, B_y, and B_z are the biases; and A_{yx}, A_{zx}, A_{xy}, A_{zy}, A_{xz}, and A_{yz} are the cross-sensitivities.

C. Thermal Calibration

Due to the thermal sensitivity of the silicon, thermal variations result in large drifts in the output value of MEMS capacitive accelerometers. There are two main approaches to reduce this effect: to reduce its causes or to compensate for them. There are also two distinctive options to reduce the source of thermal drifts: tuning or using alternative sensing structures [19], or isolating the sensor from external thermal variations [20]. However, these techniques are not feasible as a solution to improve the performance of inertial measurement units as an end user. Therefore, thermal calibration is key to improve the reliability of MEMS capacitive accelerometers.

Given the causes of thermal drifts can be related to manufacturing imperfections, each accelerometer has to be individually calibrated. Multiple techniques have been proposed to model the thermal drifts in MEMS capacitive accelerometers and compensate for them. Most, if not all of them, rely on analyzing the output value while the accelerometer is tested at different temperatures. The model and technique used to characterize the data and compensate vary among authors: polynomial curves, neural networks, polynomial surfaces, and custom equations have been proposed [21], [22], [23].

In this work, (3) is used to model the thermal drift. Therefore, the compensation technique only requires two characteristic parameters: the thermal drift of bias, TDB, and the thermal drift of scale factor, TDSF. The real acceleration value can be calculated using these two parameters, the raw acceleration, X_0; and the thermal difference from the thermal reference (25 °C), ΔT. This technique has been shown to significantly reduce thermal drift in capacitive accelerometers and requires little computing power to perform the compensation in real time, which makes it an interesting solution for IoT or wearable devices [3]. The characteristic parameters can be obtained by analyzing the relation between the thermal variation and the acceleration drift in multiple orientations [24]

$$X = X_0 + (\mathrm{TDB} + \mathrm{TDSF} \cdot X_0) \cdot \Delta T. \tag{3}$$

D. Creep

Another effect that has been analyzed because of its relevance in monitoring applications is bias instability. One cause of this effect can be related to creep in the sensing structure. Creep has been widely researched in other MEMS fields, such as RF devices, and has been found to be relevant even with

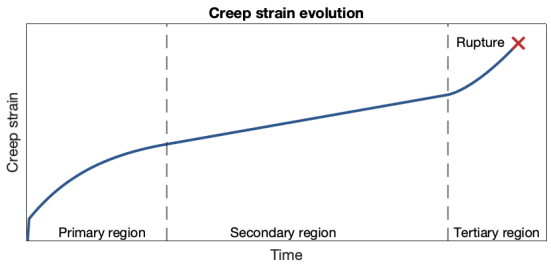

Fig. 1. Typical evolution of creep.

relatively low temperatures, such as 60 °C [25], [26]. These creep effect has been found to be accelerated with temperature and generate capacitance mismatches that reduce the sensors performance, requiring further calibrations [27].

A typical creep curve has three phases, which are represented in Fig. 1. The primary region or transient creep region, is characterized by a decreasing creep rate as a result of strain hardening. The second region or linear region, is achieved when the opposing effects of strain hardening and recovery balance each other out, causing a linear strain for a long period of time. In the tertiary region, internal cracks and cavities in the structure lead to an increase in strain rate and, ultimately, failure [6].

III. Methodology

A. Proposed Test

This work proposes a characterization test that can be used to analyze multiple parameters of the sensor. However, before the start of the test itself, the accelerometers stay at 25 °C between 12 and 24 h to ensure that effects related to the startup sequence or the initial self-heating are reduced to a level that does not interfere with the proposed analysis.

The proposed test consists of three phases; during the first phase, a mechanical calibration is performed using six orthogonal orientations and the gravity vector as reference. This phase is carried out at a controlled temperature of 25 °C, and each orientation is maintained between 40 and 60 min. This calibration is used to obtain the biases, sensitivities, and nonorthogonalities of the axes before the thermal stresses caused by the next phase of the test.

During the thermal characterization phase, a combination of Soak and Ramp methods is used [28]. At first, the temperature is stable at 25 °C for 4 h; after that time, the chamber temperature increases at approximately 0.58 °C per minute for 1 h, reaching the maximum temperature of the test: 60 °C. This temperature is maintained for another 4 h, and then it decreases again to 25 °C at a rate of −0.58 °C per minute. After another 4 h at the reference temperature, it gets lowered again at the same rate until it reaches −10 °C. The temperature remains at −10 °C for four more hours and then returns, at the same rate, to 25 °C. Four hours after the 25 °C mark has been reached for the last time, the thermal analysis for that face is concluded. The duration of each of these segments is 24 h. Once one face has been analyzed, the device under test (DUT) is rotated so that another axis faces the gravity vector, and the thermal cycle is performed again until all six orthogonal orientations have been analyzed.

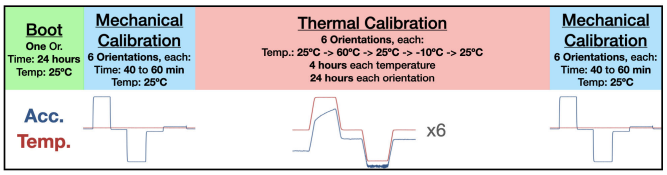

Fig. 2. Test phases. This test is performed before and after the soldering process.

When the thermal analysis is complete, another mechanical calibration is performed at 25 °C, identical to the first one. These two mechanical analysis are used to determine the permanent effects that the thermal segments induce on the accelerometer. The full sequence of the test is represented in Fig. 2.

This test will be performed twice for every unit: before and after the soldering process. By comparing the results of both tests, the influence of the soldering process on multiple characteristic parameters and the overall performance of the sensor can be studied.

B. Test Hardware

1) Accelerometer: The accelerometer tested is the LIS3DSH manufactured by STMicroelectronics. Every sensor tested is "out of the box" and has never been used before. Data are obtained via serial peripheral interface (SPI) to an Arduino Zero and then transferred via universal serial bus (USB) to a computer, where it is logged. No preprocessing is performed in any of these steps. The stored information includes the time since the test started, the raw acceleration on all three axes and the temperature provided by the accelerometer. In operation, the tested accelerometers are configured with the ±2 g scale, an output data rate of 3.125 Hz and the antialiasing filter at 50 Hz.

2) Printed Circuit Board: According to manufacturers, the design of the printed circuit board (PCB), influences the accelerometer performance and characteristics. Therefore, to achieve the optimal performance some aspects have to be taken into consideration. The PCBs used during these tests have been designed according to recommendations provided by manufacturers [12].

1) The footprint design has to be symmetrical and have the traces leave the pads straight for a couple of millimeters to reduce mechanical stress.
2) The sensor should not be placed directly in the intersection between anchor points, this reduces the mechanical stress induced to the device.
3) The sensor should not be placed outside the perimeter defined by the anchor points, in order to avoid vibrations.
4) The sensor has to be placed away from heat sources such as microcontrollers and power modules.

Following these recommendations, a PCB was designed and manufactured, Fig. 3. It also has multiple characteristics to allow different tests to be performed in the future. In addition, it includes anchor points to allow a socket to be attached and use the same footprint as the sensor.

3) Test Socket: To study the effects that the soldering process has on the performance of these sensors, each unit

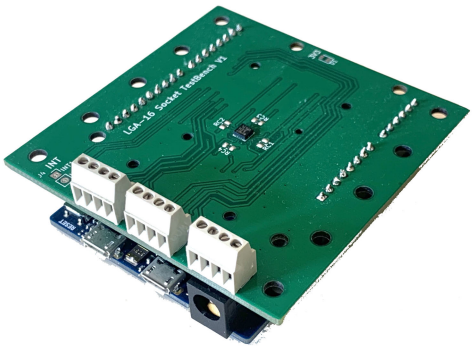

Fig. 3. Printed circuit board used for testing.

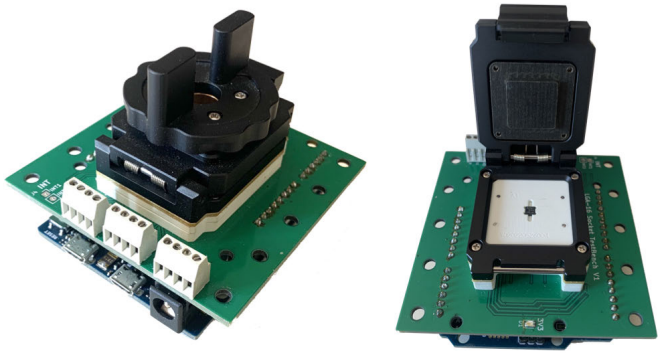

Fig. 4. Test Socket used for testing before the soldering process.

has to be analyzed unsoldered. Therefore, a test socket that allows access to the pads and locks the sensor in place without soldering is required, Fig. 4. The socket was custom made for this project and its manufacture was commissioned to an external company. Several factors were taken into account during its manufacture, including the temperatures required, the presence of a locking mechanism and the use of retractable pins to ensure the contact between the sensor and the exposed pads of the PCB at all times.

4) Soldering Process: The soldering process performed between both tests is carried out using an infrared oven and lead-free solder paste (Cobar SAC3-OT2 Sn96.5Ag3Cu0.5). The soldering curve proposed by the manufacturer was programed into the oven and monitored with external equipment to ensure the correct temperature values and gradients.

The soldering recommendations provided by manufacturers include [10], [11], [12] as follows.

1) *Preheat phase:* 150 to 200 °C - 60 to 120 s.
2) *Ramp up:* max 3 °C/s.
3) *Liquidus Time:* Above 217 °C - 60 to 120 s.
4) *Soldering Time:* Above 255 °C - 10 to 30 s.
5) *Time to max Temp.:* 25 to 260 °C - less than 480 s.
6) *Ramp down:* max 4 °C/s.

However, also in accordance with the manufacturer's recommendations, the soldering profile was adjusted during the early stages of this work. The final profile includes some changes from the manufacturer recommendations previously listed. The most relevant change is the slight decrease of some temperatures, aimed at reducing the thermal stress on the

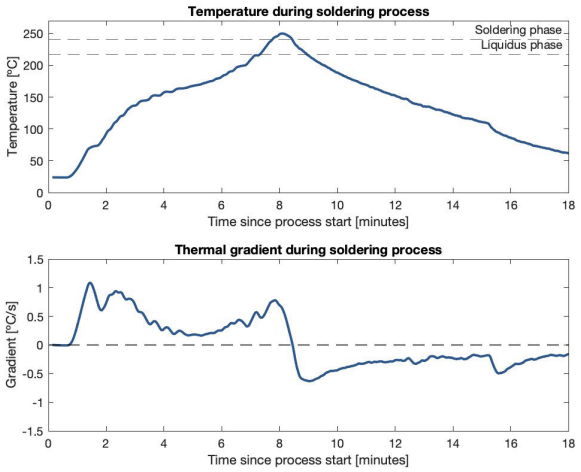

Fig. 5. Temperature profile used for soldering the sensors.

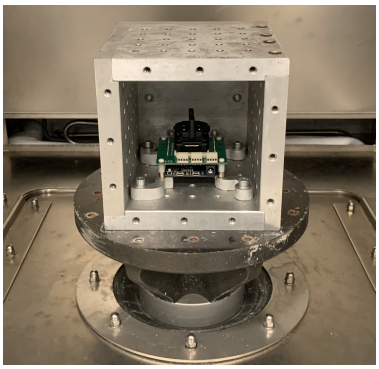

Fig. 6. Orthogonal dice, with one sample in the socket, on the testing platform inside the climatic chamber.

device. The final soldering curve and the resulting gradients are shown in Fig. 5.

5) Equipment: To carry out the experiments, the DUT, either in the socket or soldered on the PCB, is placed in an orthogonal dice, Fig. 6, to ensure the orthogonality of the six test orientations and repeatability among tests.

All the tests are carried out inside a climate chamber (FITOCLIMA 500 EDTU) to control the temperature and humidity during the tests, Fig. 7. The humidity is set to 5% at all times. The DUT is placed on a platform that is not directly connected to the climatic chamber, thus reducing significantly the propagation of vibrations produced by the chamber, to the unit being tested.

IV. Test Processing

The data recorded during the tests are slightly filtered before the proper analysis of the performance and characteristics. An exponential filter ($\alpha = 0.05$) and a glitch filter are used to reduce the noise and allow for a better analysis.

A. Thermal Characterization

During the tests, the effects of temperature over the output value produced by the sensor can be seen in every thermal step, as shown in Fig. 8. Two different effects are taking place simultaneously: the thermal drift and the creep. The thermal

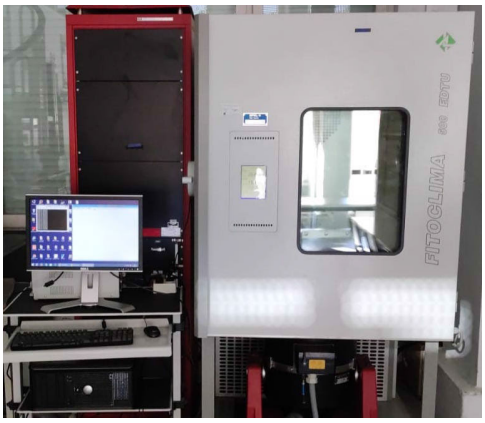

Fig. 7. Computer logging the tests (left), Thermal Chamber (right), and base of the platform where the DUT are placed (below the thermal chamber).

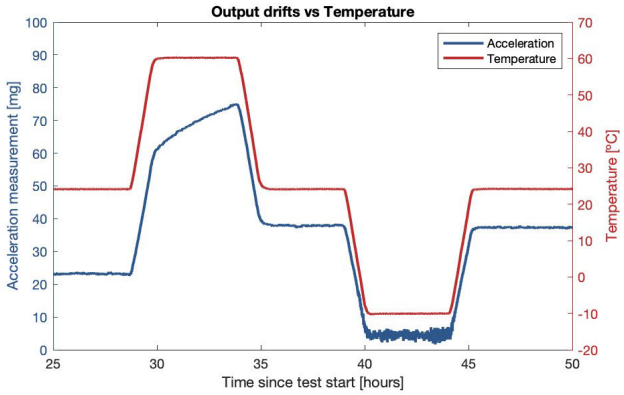

Fig. 8. Acceleration measurement (blue) and temperature (red) in one orientation for the first sample during the first test.

drift is the effect that directly relates temperature variations to acceleration drifts. The creep also induces drifts in the output value, but these appear when the sensor is exposed to high temperatures, even without thermal variations.

1) Creep: The creep is the first effect that is analyzed, as the drifts it generates are permanent and influence the remaining segments of the test. However, since it is only present during the high-temperature segments, the creep can be characterized by analyzing only those segments of the tests. Analyzing segments with the same temperature implies that no thermal drift should be present; therefore, the remaining acceleration drifts are attributed to creep.

In this work, the 60 °C segments of the test are analyzed sequentially, merging the segments and showing only the acceleration variations, the effect shows a decreasing rate of drift; where each segment start with the same slope on which the last segment ended, even when these segments took place more than 24 h apart and the orientation had been changed. This suggests that the observed creep effect is not related to electronic behaviors, but to the sensing structure.

Since the effect decreases as time progresses, it can be assumed that the sensor is in the primary region of the creep effect. In this work, this behavior is modeled using the Kelvin–Voigt equation; however, since the initial stress and the modulus of elasticity are not known, both terms are substituted with C_m, the maximum creep in (4). The creep drift after a t time at 60 °C is represented by $C(t)$; τ represents the retardation time. Similar techniques have been used to analyze creep in other MEMS devices [29], [30], [31]

$$C(t) = C_m \cdot (1 - e^{(-t/\tau)}). \tag{4}$$

The C_m and τ values are obtained with a least-square fit, allowing this effect to be modeled. The permanent drifts caused by creep can then be compensated for, before both the thermal and the mechanical calibrations, in order to remove its effect from the remaining analysis. In real applications, this compensation of creep may not be of interest, since by the time the effect has been properly characterized, its effects might be almost negligible and compensation is no longer needed.

2) Thermal Drift Calibration: After the creep compensation, the remaining acceleration drifts are considered to be related only to the thermal drift of bias and thermal drift of scale factor. Characterization of the thermal parameters, TDB and TDSF, is carried out by analyzing the relation between the temperature and acceleration variations, TD in (5), for every tested orientation. The obtained TD parameters can then be used to determine TDB and TDSF according to (6) [3]. Although multiple ways to compute the TDB and TDSF parameters can be used, two linear fits are used during this work to improve accuracy. The thermal drifts will be analyzed and compensated for, before the mechanical calibration, according to the following equation, which was derived from the model described in (3):

$$\mathrm{Acc} = \mathrm{Acc}_0 + \mathrm{TD} \cdot \Delta T \tag{5}$$

$$\mathrm{TD} = \mathrm{TDB} + \mathrm{TDSF} \cdot \mathrm{Acc}_0 \tag{6}$$

$$X_0 = \frac{X - \mathrm{TDB} \cdot \Delta T}{1 + \mathrm{TDSF} \cdot \Delta T}. \tag{7}$$

B. Mechanical Calibration

The mechanical calibration phases performed before and after each test are to obtain the bias vector and the nonorthogonality and sensitivity matrix described in (1) and (2) [32]. The parameters for both phases are computed, this way the permanent changes that bias, sensitivity and nonorthogonality undergo during the test can be analyzed. Using (8), the calibration parameters of the matrix M can be computed using the measured accelerations A, and the real accelerations U for the six tested orientations [33]

$$M = (AA^T)^{-1}A^T U. \tag{8}$$

Since mechanical calibration was always performed at 25 °C, thermal compensation should not affect it. However, if this calibration was to be performed at a different temperature, it is recommended to be computed after the thermal calibration. This is due to the fact that thermal drifts affect each axis individually, while the mechanical calibration combines data from all axes; therefore, it should be performed afterward.

To ensure that the nonorthogonalities and sensitivities can be compared among different sensors and tests, three rotations are applied to the nonorthogonalities and sensitivities matrix. These rotations are aimed at achieving zeros in the A_{yx}, A_{zx}, and A_{zy} position. This results in a matrix where only three

parameters are necessary to fully represent the nonorthogonalities, allowing for an easier comparison among units. The removed information is the relative rotation of the sensor to the reference axes, which is not a characteristic parameter of the accelerometer, and therefore will not be studied in this work. The three rotations performed, α (around X axis), β (around Y axis), and γ (around Z axis) are computed as shown in (9)–(11)

$$\alpha = \arcsin(A_{zy}) \tag{9}$$

$$\beta = -\arcsin\left(A'_{zx}\right) \tag{10}$$

$$\gamma = \arcsin\left(A''_{yx}\right). \tag{11}$$

Note that the parameter A'_{zx} used to compute β is the one remaining in the matrix after the first rotation (using α), not the original value. Similarly, γ should only be computed, using A''_{yx}, after the rotations α and β.

Note that the parameters presented in Section V are those obtained using the second segment of mechanical calibration, since it is the one that better represents the behavior during operation.

C. Performance Analysis

1) Absolute Error: To determine the performance of the sensors, the maximum absolute error is computed for each sensor. This error is calculated as the maximum range of output values that the sensor generates without a change in the actual acceleration; as represented in (12). Therefore, it represents the maximum expected error in an application with similar conditions as the proposed test regarding thermal variations

$$E = \max(X) - \min(X). \tag{12}$$

For each thermal segment, the absolute error is computed in all four combinations of possible compensations: with and without creep compensation and thermal compensation. This helps to determine how much each of these effects influence the performance of the sensors.

2) Uncertainty: Another major characteristic that can be studied in any kind of sensor is its uncertainty, which measures the reliability of a sensor and should be taken into account when performing any kind of measurement. Similar to the maximum errors, the uncertainty will be computed in different scenarios of compensation to determine its sources.

The uncertainty of the measurements, u, can be calculated in the same way as the standard deviation, σ, of the measurements, (13). The calibration equipment uncertainties, or any other uncertainty source, can also be taken into account using the combined uncertainty, (14). The expanded uncertainty U, showed in (15), allows for the combined uncertainty to represent a larger percentage of cases, which is controlled with the coverage factor k. A value of 2 represents 95% of cases, while $k = 3$ represents 99% of cases

$$u = \sigma = \sqrt{\frac{1}{N}\sum_{i=1}^{n}(x_i - \bar{x})^2} \tag{13}$$

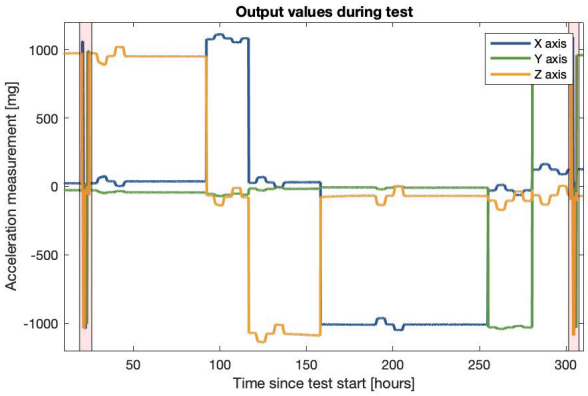

Fig. 9. Acceleration measurements in all three axes during the first test of the first sample. X axis is represented in blue, Y in green, and Z in yellow. Both calibration phases have been highlighted in red at the edges of the plot.

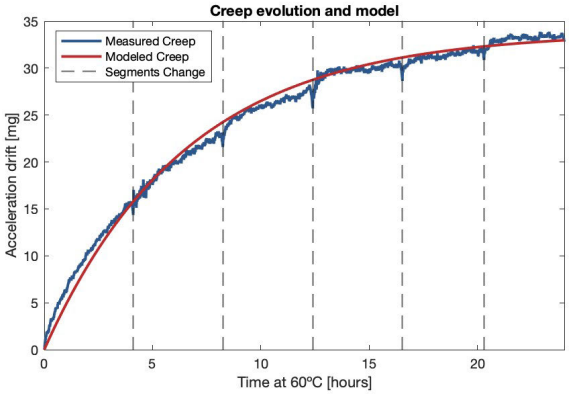

Fig. 10. Creep experimental values, in blue, during the first test of the first sample, merging the 60 °C segments, and fit model in red. Some mismatches are visible in the merging points, but the overall trend is clear.

$$u_c = \sqrt{\sum_{i=1}^{n} u_i^2} \tag{14}$$

$$U = k \cdot u_c. \tag{15}$$

V. Results

A. Overview

An example of the raw data that is logged during one of these tests is shown in Fig. 9, where both mechanical calibration phases have been highlighted. The six orientations and the effects of temperature in the acceleration measurements are also clearly visible during the test.

B. Thermal Analysis

1) Creep: The fit of the merged segments to compute the creep characteristic parameters according to (4) is shown in Fig. 10. Data obtained by analyzing all samples are summarized in Table I.

According to the five unsoldered samples tested and the test conditions (60 °C), the creep ranges from −77 to +87 mg with an average value of −1.7 mg. This indicates that the creep does not have a preferred direction; however, the average absolute value was higher than 35 mg. This can lead to significant

TABLE I
VALUES OBTAINED FOR THE CREEP MAXIMUM VALUE AND RETARDATION TIME

Parameter	Test	Min	Max	Avg. Abs.	Avg.
C_m $[mg]$	Unsoldered	-77.3	86.7	37.2	-1.7
	Soldered	-89.3	82.2	42.5	-5.1
	Variations	-23.6	21.1	8	-3.4
τ $[h]$	Unsoldered	4.56	8.76	-	6.76
	Soldered	5.55	12.68	-	8.15
	Variations	-3.2	4.51	2.11	1.38

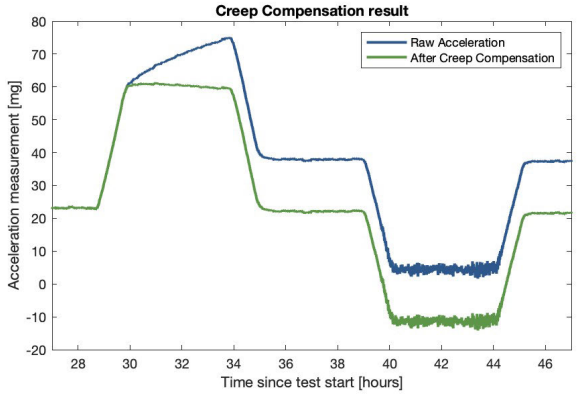

Fig. 11. Raw acceleration measurements, in blue, and acceleration measurements after creep compensation, in green, in the first thermal step from the first test of the first sample. The full acceleration series is affected due to the permanent nature of the drifts caused by creep.

errors in any high accuracy measurement equipment if not taken into consideration during measurements. The soldered tests showed similar results in terms of amplitude; in fact, the average variation between the unsoldered and soldered tests was only 8 mg, although some units reached a variation larger than 20 mg. Overall, the measured creep values are in the $\pm$90 mg range.

The τ average value before soldering is 6.76 h; therefore, the creep will reach 90% of its maximum value after 15.5 h at 60 °C, and only reach stability (99% of its maximum value) after 31 h.

The retardation time of the soldered tests was considerably higher, with an average τ increase of 20%. This increment was 1.38 h with an average variation of 2.11 h. However, some units lowered their τ value, indicating that their creep retardation time decreased. In the sample with the largest retardation time ($\tau = 12.68$), the stabilization times reached up to 29 h for 90%, and 58 h for 99% of the maximum creep.

As explained previously, this effect may not be compensable in operation, since its effects are reduced to low levels of drift by the time it has been properly analyzed. The effect is characterized and compensated for during this work in order to better analyze other thermal effects. Fig. 11 shows one thermal segment before and after the creep compensation.

Regarding the expression used to model the creep at constant temperature (4), the results are quite satisfactory; the average R^2 of the fit was 0.992, with the minimum being 0.951. Therefore, the model proposed seems to be a good representation of the creep and a viable compensation technique, at least in those cases where it could be compensated for.

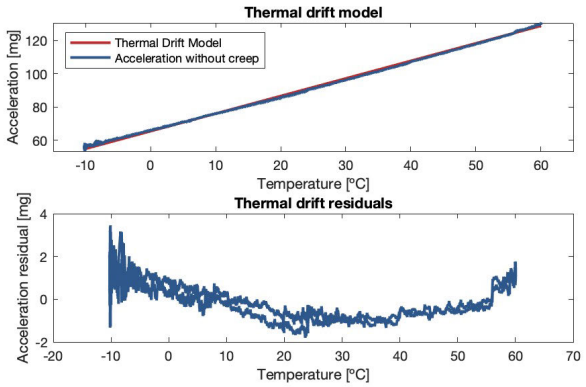

Fig. 12. Fit for the *TD* ratio for a single orientation (above) and residuals of the fit (below). One of these fits has to be performed for each orientation in order to obtain all the desired *TD* values.

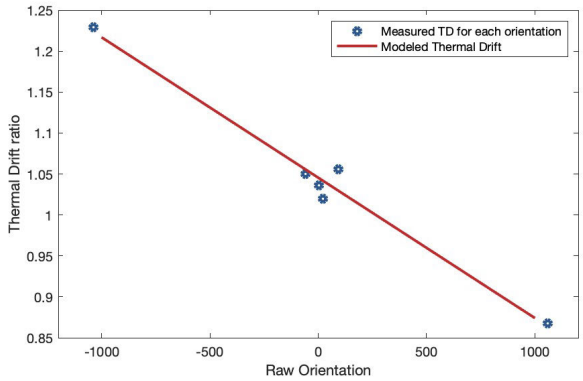

Fig. 13. Fit to obtain the TDB and TDSF from the thermal drift ratios, *TD*, and the raw orientations.

TABLE II
THERMAL DRIFT CHARACTERISTIC PARAMETERS

Parameter	Test	Min	Max	Avg. Abs.	Avg.
TDB	Unsoldered	-2.59	1.28	0.90	-0.32
$[mg/°C]$	Soldered	-2.50	1.27	0.92	-0.32
	Variations	-0.083	0.088	0.037	0.002
$TDSF$	Unsoldered	-187	-5	-	-76
$[ppm/°C]$	Soldered	-185	-2	-	-72
	Variations	-122	87	32	-4

2) Thermal Drifts: Once the creep effect has been removed, the remaining output drifts related to temperature can be attributed to thermal drifts. As explained in Section IV-A2, the first step of this analysis consists of obtaining a TD parameter for each individual orientation and test. This is achieved with a least square regression to (5). The result of one these fits and its residuals are shown in Fig. 12.

For each axis, four TD values are obtained with the raw acceleration close to 0 g, one close to 1 g and one close to -1 g. When the TD values for all the desired orientations are known, the TDB and TDSF values can be computed with another fit, using also the raw acceleration, shown in Fig. 13. A summary of the obtained characteristic parameters of the thermal drift is shown in Table II.

The TDB values computed during these tests range from 1.27 to -2.5 mg/°C with an average of -0.32 mg/°C, but an absolute average of 0.92 mg/°C. An interesting result is the

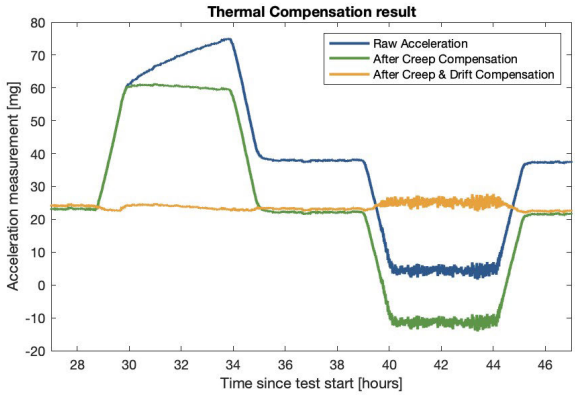

Fig. 14. Compensation example showing the raw acceleration measurement (blue), the acceleration measurement after creep compensation (green), and the acceleration measurement after creep and thermal drift compensation (yellow) in the first thermal step from the first test of the first sample.

TABLE III
BIAS VALUES (mg) OBTAINED DURING ALL FOUR CALIBRATION PHASES

	Min	Max	Avg. Abs.	Avg.
Unsold. before Test	-34.2	24.0	15.0	-7.6
Unsold. after Test	-108.4	74.9	55.3	-11.9
Soldered before Test	-20.5	50.3	15.5	8.9
Soldered after Test	-74.6	101.3	45.0	-0.2
Sold. Variations	-25.3	69.0	27.3	16.5

minimal variation this parameter experiences during the soldering process, the maximum variation was only 0.08 mg/°C and the average absolute variation was 0.03 mg/°C.

The TDSF values obtained during these experiments are all negative values, ranging from 0 to −200 ppm/°C. The variations induced by the soldering process were larger, in relative value, than the TDB, but not too significant, with an average variation on 32 ppm/°C.

These parameters can be used to compensate for a large amount of the acceleration drifts as shown in Fig. 14, where (7) was applied. Although some errors are still visible, there is clearly a great improvement in data stability.

C. Mechanical Characterization

1) Bias: The mechanical bias is a good indicator of the accuracy of these sensors, as it indicated the error at 0 g without the influence of thermal drifts or sensitivity. A summary of the bias values obtained for all units during the tests is shown in Table III.

The bias values calculated before thermal stress was applied, ranged from −34 to 24 mg. The maximum, minimum, and absolute average of these values increased more than 300% during the proposed test; arguably due to the creep effect; however, the average value remained similar, showing the randomness of the bias and creep signs.

The soldering process also generated significant bias deviations, with an average absolute variation of 40 mg. Interestingly, the bias values after the soldering process were much closer to zero, since the absolute average value was reduced from 55 to 15 mg, and the total range of values was reduced from 190 to 70 mg. The average value also changed significantly from −12 to 9 mg.

TABLE IV
SENSITIVITY VALUES OBTAINED DURING THE TESTS, SHOWN AS SENSITIVITY ERROR IN PERCENTAGE

	Min	Max	Avg. Abs.	Avg.
Unsold. before Test	-1.51	6.84	3.68	3.38
Unsold. after Test	-1.47	6.60	3.62	3.28
Test Variations	-0.09	0.27	0.14	0.10
Soldered before Test	-1.35	6.00	3.54	3.17
Soldered after Test	-1.27	5.93	3.50	3.16
Test Variations	-0.10	0.26	0.08	0.01
Sold. Variations	-0.82	0.26	0.24	-0.11

TABLE V
NONORTHOGONALITY, OR CROSS SENSITIVITY, OBTAINED DURING THE TESTS, EXPRESSED AS CROSS SENSITIVITY IN PERCENTAGE

Axes	Test	Min	Max	Avg. Abs.	Avg.
XY	Unsoldered	4.08%	4.89%	4.46%	4.46%
	Soldered	4.20%	4.61%	4.37%	4.37%
	Variations	-0.37%	0.17%	0.18%	-0.09%
XZ	Unsoldered	-0.36%	-0.14%	0.23%	-0.23%
	Soldered	-0.48%	-0.07%	0.23%	-0.23%
	Variations	-0.33%	0.17%	0.14%	0.00%
YZ	Unsoldered	-0.33%	0.45%	0.29%	0.06%
	Soldered	-0.36%	0.86%	0.36%	0.16%
	Variations	-0.24%	0.41%	0.22%	0.10%

During the soldered tests, the bias values showed variations similar to those of the unsoldered tests, and the final values were in the same range as those after the unsoldered test, ranging from −75 to 101 mg, although slightly lower in absolute average, 45 mg.

However, it should be noted that, as mentioned earlier, the retardation time of creep, τ, during the soldered tests was 20% higher on average, meaning that creep in some cases had not fully stabilized before the test ended. Therefore, if the tests had continued, the range of bias values would probably be larger.

2) Sensitivity: The sensitivity values for the axes show a greater stability when compared to the bias values. Maximum deviations from the ideal sensitivity ranged from −1.5% to 6.8%. Both these values were from unsoldered units before the test. As the tests were being carried out, the sensitivities approached the nominal value (100%): the lower sensitivities slightly increased and the higher sensitivities slightly decreased. Therefore, the average sensitivity error was slightly reduced from 3.28% to 3.16%. Average variations during tests were always lower than 0.3%, with average deviations of 0.08% and 0.14%. The soldering process did affect the sensitivity of the units more significantly, with changes up to 0.82%, although the average variation was 0.24%. A summary of the sensitivity values obtained for all units is shown in Table IV.

3) Nonorthogonalities: As previously mentioned, the nonorthogonalities matrix is rotated around all three axes to enable the comparison of the A_{xy}, A_{yz}, and A_{xz} values. The values computed after the tests are presented in Table V as percentages, where 0% represents a perfect orthogonality, and therefore no cross-sensitivity between the axes; and 100% would represent that the axes are completely parallel to each other.

The nonorthogonality values show an interesting characteristic of this sensor: the cross sensitivity is much higher

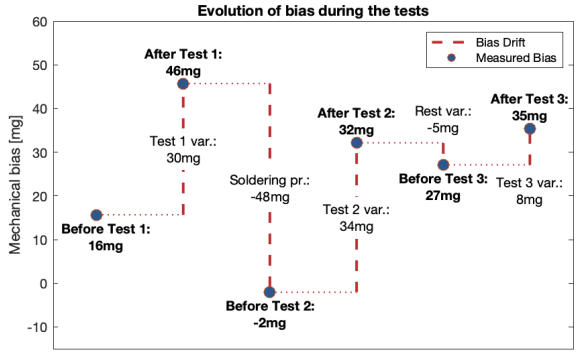

Fig. 15. Bias evolution of the *X*-axis for the first sample during multiple phases. A similar behavior is shown during tests 1 (unsoldered) and 2 (just soldered). The soldering process effect, opposite to creep, is also visible. The bias variations during the storage phase and third test are visible, although much lower in value.

between the X and Y axes (almost 4.5% on average) than between any of them with the Z axis (around 0.3% on average).

Although in all cases the cross-sensitivities remain in roughly the same ranges, 4% to 5% for A_{xy} and -0.5% to 1% for A_{xz} and A_{yz}, the soldering process has a relatively large impact on the values, with average variations around 0.15% to 0.22% and maximum variations of $\pm 0.4\%$, which has a magnitude similar to the values themselves.

4) Bias Evolution: The mechanical characteristic parameters for each sensor have been calculated four different times; however, sample 1 was tested a third time with the same experiment, once all the other tests had been completed. Between the soldered test and this third test, the unit was stored for two months at room temperature. The evolution of bias during the six mechanical calibrations performed is shown in Fig. 15.

The first point of Fig. 15 represents the starting point of the bias for the X axis of the first sample. This bias changed 30 mg during the test due to the creep. However, during the soldering process, the bias value decreased by 47 mg, reaching a value lower than the original before the first test. The second test also increased the bias value in 34 mg, from -2 to $+32$ mg, similar to the increase experienced during the first test. After this second test, the unit was left at room temperature for two months; in this time, the bias value slightly decreased by 5 mg. The third test showed a much lower creep compared to the other two tests, causing a bias increase of only 8 mg.

D. Performance

1) Maximum Error: The average maximum error in the measurements before and after each compensation technique, according to (12) is shown in Table VI. Different states of compensation of creep and thermal drift are shown, as well as different segments. The first and last segments are used to illustrate the reduction in error as creep reaches a more stable state.

The average error before and after soldering is around the same values, 70–80 mg. It is slightly higher in the tests with soldered units, 3 mg, but is not considered a significant deviation. The creep effect is also an important factor in the performance of the sensor; as seen in Table VI, the maximum error consistently decreases as the tests progress and creep stabilizes. The uncompensated error decreases an average of 8 mg, and the error after the drift compensation decreases even more, between 14 and 16 mg, which represents approximately 66% of the error at that point.

TABLE VI
AVERAGE ERRORS (mg) IN DIFFERENT CASES

Test	Segment	Uncomp.	Drift Comp.	Drift & Creep
Unsold.	First	76.07	24.90	10.93
	Avg.	70.12	13.00	8.19
	Last	68.19	8.69	7.19
Soldered	First	79.63	22.60	9.93
	Avg.	72.84	11.91	7.48
	Last	71.65	8.46	7.02

TABLE VII
MAXIMUM ERRORS (mg) IN DIFFERENT CASES

Test	Segment	Uncomp.	Drift Comp.	Drift & Creep
Unsold.	First	167.55	49.72	20.53
	Avg.	179.78	23.81	13.61
	Last	184.68	14.45	14.43
Soldered	First	164.77	43.02	24.10
	Avg.	175.07	21.94	10.71
	Last	180.21	14.87	13.67

The absolute maximum errors, shown in Table VII reach up to 180 mg in the most extreme cases; however, these errors are reduced to values lower than 50 mg with the thermal compensation. Out of these, similar to the average errors, also more than 66% are caused by the creep, with a difference in the maximum error of 30–35 mg between the first segment and the last one.

The maximum error after compensation and creep stabilization is in all the studied units lower than 15 mg, which represents a great improvement compared to the initial 180 mg or even the average 70 mg error.

The influence of each one of these effects is shown in Table VIII and Fig. 16. The great influence of creep in the first segment and its fast decrease is clearly visible. The soldered tests show a lower influence of creep, probably due to a higher retardation time and, therefore, slower progress. The error attributed to thermal drifts shows an increase around 5%–10% both as tests progress and during the soldering process. The residual error, that could not be compensated with these compensations, remains with little change around 10 mg in the first stages of tests, and is reduced to 7 mg by the end of them.

2) Uncertainty: The uncertainty of the sensors measurements, calculated as in (13), is presented in Table IX. It should be noted that the uncompensated uncertainty may not be a reliable value to compare with other work, as it is highly dependent on test times and temperature variations. However, it can be used as an indicator of performance improvement.

The uncertainty of the calibration tests, where the only cause of uncertainty is the noise of the sensors, is around 0.6 mg. This value reaches an average of 1.15 mg when computing the uncertainty of the segments with compensated thermal variations. For comparison, the average uncertainty of the tests

TABLE VIII
ERRORS (mg) BY SOURCES IN DIFFERENT SCENARIOS, AVERAGED AMONG ALL UNITS

Test	Segment	Creep	Drift	Other
Unsold.	First	13.97	51.17	10.93
	Avg.	4.81	57.12	8.19
	Last	1.49	59.50	7.19
Soldered	First	12.67	57.03	9.93
	Avg.	4.43	60.93	7.48
	Last	1.45	63.19	7.02
Variation	First	-1.30	5.86	-0.99
	Avg.	-0.39	3.81	-0.70
	Last	-0.05	3.69	-0.18

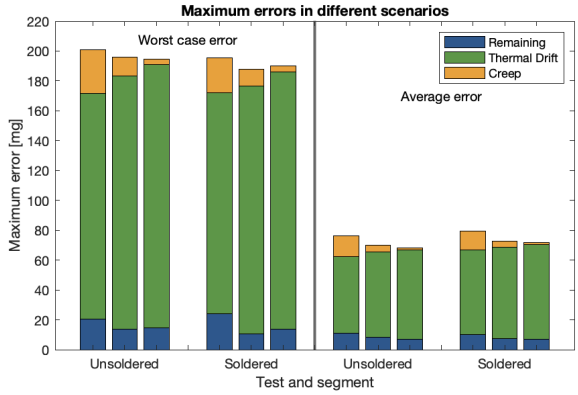

Fig. 16. Maximum errors and their causes during the different tests and segments. Each three bars represent the first, average, and last segments of the corresponding tests, this way the evolution of creep and thermal drift errors is clearly visible.

TABLE IX
SENSORS UNCERTAINTY (mg) IN DIFFERENT CASES

Test	Uncomp.	Thermal Drift Comp.	Drift and Creep Comp.	Calibration Segment	Calibration Equipment
Unsold.	3.70	1.69	1.19	0.62	0.028
Sold.	3.94	1.62	1.11	0.56	0.028

without the creep or drift compensation reaches up to 1.7 and 3.8 mg, respectively, with the current conditions.

In addition, the uncertainty of the calibration equipment has been taken into account, but its value represents less than 5% of the total uncertainty; therefore, it is considered of no significance to these tests results. Overall, the extended uncertainty taking into account the equipment uncertainty is 2.29874 mg, computed as shown in (15), and 2.29806 mg when the equipment is considered ideal, which represents only a 0.68 μg increment. A graphic representation of the uncertainty in different cases is shown in Fig. 17.

VI. ANALYSIS/DISCUSSION

A. Characteristic Parameters Estimation

1) Thermal Characteristics: The creep effect, clearly visible in all tests during the heating segments, could be properly modeled according to (4), even with the merged segments. The data fits to this model show that creep has a range of $\pm$90 mg and may generate a significant error in any kind of application. The stabilization time of the creep is dependent on temperature. In the conditions set up for this work, it was found to be around 37 h, with maximum stabilization times of 58 h.

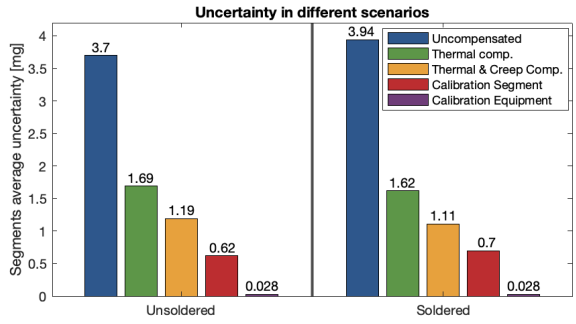

Fig. 17. Average uncertainty values during the tests, including the calibration equipment.

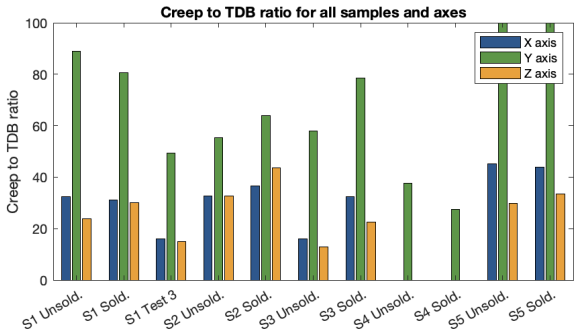

Fig. 18. Relation between the Creep and TDB Values (Not showing those with TDB lower than 0.1 mg/°C). Each group represents the axes of one sample (S) in one test.

The computed values of TDB and TDSF match those of previous studies and theoretical works; with TDB in a typical range of $\pm$1.5 mg/°C but reaching up to $\pm$2.5 mg/°C. The TDSF value was always negative, in the range of $0-200$ ppm/°C.

It should be noted that, if the parameters TDB and C_m are compared, as in Fig. 18, an interesting pattern can be observed. The TDB and the C_m sign is the same for all samples with a TDB larger than 0.1 mg/°C, lower values are not considered reliable for this comparison. The sign of the C_m/TDB relation is always positive, but the value is random, usually between 15 and 50, although some values are much higher, probably due to a lower TDB. This relation suggests that the Creep and TDB effects could be influenced by the same thermal and mechanical characteristics of the sensing structure.

2) Mechanical Characteristics: The bias value changed significantly during the tests, with its values in the $\pm$100 mg range. However, the bias range was larger after the tests, since it includes the permanent effect of the creep. The average variations both during the soldering phase and the thermal test was around 40 mg.

The average sensitivity of the axes was found to be, on average, slightly larger than the ideal 100%, with values between 98.5% and 106.8%. These values were slightly closer to the ideal value after the soldering process and the tests.

The cross-sensitivity parameters show a different behavior between the XY axes and the XZ or YZ axes. The XY pair of axis shows a significant cross-sensitivity, probably due to the fact that the X and Y axes are manufactured orthogonal to

each other and in the same sensing structure. In contrast, the XZ and YZ pairs have a much lower cross-sensitivity, perhaps caused by the Z axis ensuring its orthogonality by using an alternative sensing technique.

B. Soldering Process Effects

The soldering process and PCB design are considered by many manufacturers an important factor in the sensors performance. In this work, the soldering and PCB design recommendations were followed, and the results after both tests indicate that all parameters suffer some degree of variation during the soldering process. The most stable characteristic was the TDB, with all variations lower than 0.09 mg/°C. The TDSF showed some larger variations, but the overall values remained in the same range. The sensitivities and nonorthogonalities also showed a high stability in absolute values, with variations in the ±0.5% range both in the axis sensitivity and cross-sensitivity. However, these variations can be considered significant deviations when taking into account the actual values of sensitivities and nonorthogonalities.

The factors that were most influenced by the soldering process were mechanical bias and creep, both in maximum value and retardation time. The maximum value of the creep did not change as significantly; however, the effect appeared to start again as if it had not happened before. In fact, the bias change direction during the soldering process was always opposite to the creep. After the soldering process, the creep effect started again as if it had never been tested, although in that cases, the retardation times showed a 20% increase on average; interestingly, the retardation time for some of the sensors also decreased.

C. Third Test-In Operation

Comparing the characteristic parameters of the first sample after the second test with those of the third test, many parameters remain similar, such as TDB, TDSF, and sensitivity. The bias changed slightly during the months at room temperature, drifting opposite to the creep. However, the creep maximum value during the third test decreased to half of the original value (tests 1 and 2) in all three axes. It seems that the mechanical bias was still affected by creep, but in the absence of high temperatures, it tended to drift back to a stable position closer to zero. However, the new segments of high temperature induced creep again, although lower in magnitude, since most of the original creep deviations were still present in the device.

D. Performance

The maximum error, calculated as (12), was 70 mg on average with maximum errors up to 180 mg. These values could represent a real problem and significantly reduce the potential use of these sensors in variable temperature environments. Once the creep has stabilized, or has been compensated, and the thermal drift is compensated, the maximum errors were reduced to 7 mg on average, with a 14 mg maximum.

The main source of error during the tests was the thermal drift. However, during the first segment, the creep generated 14 mg of error on average, and up to 30 mg in worst tested case. As the tests progress the creep effect was reduced; furthermore, the thermal drift seemed to fit better, achieving better compensation and lower overall errors. This suggests that the thermal drifts compensation model has a better accuracy when no creep is present and that creep could be a real issue before its stabilization. Also, thermal drifts seem to increase their effects as tests progress; however, this is probably just a consequence of a better fit of the model due to the reduction of creep. Alternatively, this could be due to some kind of interaction between both effects that is not modeled with the proposed techniques, but more research should be done before drawing conclusions.

The uncertainty of the sensor during the uncompensated phases might not be a reliable indicator as explained previously. However, its value is significantly higher than those obtained for the compensated or calibration segments. The thermally compensated segments achieve a significantly reduced uncertainty, the average value was 1.1 mg, while the reference segment was 0.7 mg. This increment might still be relevant for high precision applications, but is a great improvement that allows for low-cost sensors to be used in many applications with variable temperatures.

VII. Conclusion

Many characteristic parameters of MEMS capacitive accelerometers, and their evolution, have been analyzed during tests with thermal steps. The influence of the soldering process on these parameters has been also studied. The results show that, while some characteristic parameters remain almost constant for the whole duration of the tests, others show interesting variations in different phases of the tests. The ranges and relative variations of these characteristics, both during the soldering process and the tests, have been identified and characterized individually, allowing researchers and end users a better understanding, and therefore better use, of MEMS capacitive accelerometers.

In general, mechanical bias has proved to be the most variable characteristic during the all phases of the tests. Bias can vary significantly during the soldering process and should be calibrated afterward; moreover, it might be necessary to perform regular calibrations to achieve the best results, as bias instability and creep can lead to significant errors during applications, especially with variable temperatures.

The sensitivity and nonorthogonalities parameters showed much more stability than bias during the proposed tests. However, they still suffered some small variations during the soldering or thermal characterization phases. These were usually lower than 0.25%, but still should be taken into account in high precision applications.

The thermal characteristic parameters TDB and TDSF showed a high degree of immunity to thermal variations. This is especially relevant in the case of TDB, as it is the main cause of the thermal drift. The variations of all tested units were in the ±0.09 mg/°C range.

The lightweight thermal model proposed in previous works to compensate for the thermal drifts has been shown to significantly reduce the maximum error. The errors caused by the thermal drift, and compensated for with the proposed

technique, were found to be up to 170 mg, with an average of 60 mg. The maximum error after compensation was lower than 15 mg in all cases, and lower than 9 mg on average by the end of the tests. These compensation results indicate that the proposed technique accurately models the thermal drifts, and the remaining errors are caused by creep or other effects. These thermal drift parameters might be easier to characterize using colder temperatures, instead of hotter ones, since at high temperatures other sources of error can appear.

The creep effect during constant temperature segments has been modeled using the Kelvin–Voigt expression with successful results ($R^2 > 0.95$). Also, it was noticed that thermal drifts and creep drifts matched signs in all the tested units; therefore, both effects could be caused by the same stress; the TDB being the immediate displacement of the sensing structure, and creep being the long-term displacement.

The uncertainty and errors in different scenarios were computed, identifying the influence of each error source in performance losses. The analysis performed during this work showed that the main source of error in MEMS capacitive accelerometers is the thermal drift. Creep was also a significant source of errors; however, the creep is reduced as time progresses and by the end of the tests, its effects were almost negligible. The uncertainty values after compensation (1.2 mg) still do not reach the uncertainty values of the constant temperature segments (0.7 mg), but are a great improvement compared to the uncompensated values (3.9 mg). The uncertainties of the soldered and unsoldered tests do not show significant differences in any compensation scenario, suggesting that, by following the manufacturer recommendations in PCB layout and soldering technique, performance is maintained.

REFERENCES

[1] G. Langfelder, M. Bestetti, and M. Gadola, "Silicon MEMS inertial sensors evolution over a quarter century," *J. Micromech. Microeng.*, vol. 31, no. 8, Aug. 2021, Art. no. 084002.

[2] J. Ramakrishnan, P. T. R. Gaurav, N. S. Chandar, and N. M. Sudharsan, "Structural design, analysis and DOE of MEMS-based capacitive accelerometer for automotive airbag application," *Microsyst. Technol.*, vol. 27, no. 3, pp. 763–777, Mar. 2021.

[3] J. Martínez, D. Asiain, and J. R. Beltràn, "Lightweight thermal compensation technique for MEMS capacitive accelerometer oriented to quasi-static measurements," *Sensors*, vol. 21, no. 9, p. 3117, 2021.

[4] D. Liu et al., "In-situ compensation on temperature coefficient of the scale factor for a single-axis nano-g force-balance MEMS accelerometer," *IEEE Sensors J.*, vol. 21, no. 18, pp. 19872–19880, Sep. 2021.

[5] P. Peng et al., "Drift of MEMS capacitive accelerometers for one-year room-temperature storage: A simulation and experimental study," *IEEE Sensors J.*, vol. 23, no. 1, pp. 202–210, Jan. 2023.

[6] K. Tuck, A. Jungen, A. Geisberger, M. Ellis, and G. Skidmore, "A study of creep in polysilicon MEMS devices," *J. Eng. Mater. Technol.*, vol. 127, no. 1, pp. 90–96, Jan. 2005.

[7] F. Huber, H. Etschmaier, H. Walter, G. Urstöger, and P. Hadley, "A time-temperature-moisture concentration superposition principle that describes the relaxation behavior of epoxide molding compounds for microelectronics packaging," *Int. J. Polym. Anal. Characterization*, vol. 25, no. 6, pp. 467–478, Jul. 2020.

[8] J. Cheng and Z. Li, "Analysis of thermo-mechanical coupling damage behavior in long-term performance of microelectromechanical systems actuators," *Int. J. Damage Mech.*, vol. 31, no. 2, pp. 190–214, Feb. 2022.

[9] H. Liang, X. He, and B. Xiong, "Two-mask wafer-level vacuum packaging with bulk-Si 3D interconnects for MEMS devices and its package performances," *IEEE Sensors J.*, vol. 22, no. 14, pp. 14522–14530, Jul. 2022.

[10] *InvenSense MEMS Handling*, InvenSense, San Jose, CA, USA, 2014.

[11] I. Binda and L. Rancati, "Soldering guidelines for MEMS inertial sensors," Maxim Integr. Products, Inc., San Jose, CA, USA, Appl. Note 5604, Mar. 2013. [Online]. Available: https://pdfserv.maximintegrated.com/en/an/AN5604.pdf or http://www.maximintegrated.com/an5604

[12] *Surface Mounting Guidelines for MEMS Sensors in an LGA Package*, STMicroelectronics, Geneva, Switzerland, 2023.

[13] A. Briffa, E. Gatt, J. Micallef, I. Grech, O. Casha, and J. M. Darmanin, "Area minimization of a three-axis separate mass capacitive accelerometer using the Thelma process," in *Proc. Eurocon*, Jul. 2013, pp. 2094–2099.

[14] J. He, J. Xie, X. He, L. Du, and W. Zhou, "Analytical study and compensation for temperature drifts of a bulk silicon MEMS capacitive accelerometer," *Sens. Actuators A, Phys.*, vol. 239, pp. 174–184, Mar. 2016.

[15] Y. Furubayashi et al., "A 22-ng/$\sqrt{}$Hz 17-mw capacitive MEMS accelerometer with electrically separated mass structure and digital noise-reduction techniques," *IEEE J. Solid-State Circuits*, vol. 55, no. 9, pp. 2539–2552, Sep. 2020.

[16] P. Zwahlen et al., "Breakthrough in high performance inertial navigation grade sigma-delta MEMS accelerometer," in *Proc. IEEE/ION Position, Location Navigat. Symp.*, Apr. 2012, pp. 15–19.

[17] M. Sipos, P. Paces, J. Rohac, and P. Novacek, "Analyses of triaxial accelerometer calibration algorithms," *IEEE Sensors J.*, vol. 12, no. 5, pp. 1157–1165, May 2012.

[18] W. T. Fong, S. K. Ong, and A. Y. C. Nee, "Methods for in-field user calibration of an inertial measurement unit without external equipment," *Meas. Sci. Technol.*, vol. 19, no. 8, Aug. 2008, Art. no. 085202.

[19] J. He, W. Zhou, H. Yu, X. He, and P. Peng, "Structural designing of a MEMS capacitive accelerometer for low temperature coefficient and high linearity," *Sensors*, vol. 18, no. 2, p. 643, Feb. 2018.

[20] D. Yang, J.-K. Woo, S. Lee, J. Mitchell, A. D. Challoner, and K. Najafi, "A micro oven-control system for inertial sensors," *J. Microelectromech. Syst.*, vol. 26, no. 3, pp. 507–518, Jun. 2017.

[21] B. Qi, S. Shi, L. Zhao, and J. Cheng, "A novel temperature drift error precise estimation model for MEMS accelerometers using microstructure thermal analysis," *Micromachines*, vol. 13, no. 6, p. 835, May 2022.

[22] G. Ruzza, L. Guerriero, P. Revellino, and F. M. Guadagno, "Thermal compensation of low-cost MEMS accelerometers for tilt measurements," *Sensors*, vol. 18, no. 8, p. 2536, Aug. 2018.

[23] T. Xu, X. Xu, D. Xu, Z. Zou, and H. Zhao, "Low-cost and efficient thermal calibration scheme for MEMS triaxial accelerometer," *IEEE Trans. Instrum. Meas.*, vol. 70, pp. 1–9, 2021.

[24] J. Martínez, D. Asiain, and J. R. Beltrán, "Self-calibration technique with lightweight algorithm for thermal drift compensation in MEMS accelerometers," *Micromachines*, vol. 13, no. 4, p. 584, 2022.

[25] M. van Gils, J. Bielen, and G. McDonald, "Evaluation of creep in RF MEMS devices," in *Proc. Int. Conf. Thermal, Mech. Multi-Physics Simul. Experiments Microelectron. Micro-Syst.*, 2007, pp. 1–6.

[26] A. Somà, M. M. Saleem, and G. de Pasquale, "Effect of creep in RF MEMS static and dynamic behavior," *Microsyst. Technol.*, vol. 22, no. 5, pp. 1067–1078, May 2016.

[27] X. Huang, X. Dong, G. Du, and Y. Hu, "Long-term degradation evaluation of the mismatch of sensitive capacitance in MEMS accelerometers," *Micromachines*, vol. 14, no. 1, p. 190, Jan. 2023.

[28] X. Niu, Y. Li, H. Zhang, Q. Wang, and Y. Ban, "Fast thermal calibration of low-grade inertial sensors and inertial measurement units," *Sensors*, vol. 13, no. 9, pp. 12192–12217, Sep. 2013.

[29] H.-H. Hsu and D. Peroulis, "An experimental investigation on viscoelastic behavior in tunable planar RF-MEMS resonators," in *IEEE MTT-S Int. Microw. Symp. Dig.*, May 2010, pp. 1150–1153.

[30] H.-H. Hsu and D. Peroulis, "A viscoelastic-aware experimentally-derived model for analog RF MEMS varactors," in *Proc. IEEE 23rd Int. Conf. Micro Electro Mech. Syst. (MEMS)*, Jan. 2010, pp. 783–786.

[31] M. McLean, W. L. Brown, and R. P. Vinci, "Temperature-dependent viscoelasticity in thin Au films and consequences for MEMS devices," *J. Microelectromech. Syst.*, vol. 19, no. 6, pp. 1299–1308, Dec. 2010.

[32] R. Wei et al., "A research on calibration of low-precision MEMS inertial sensors," in *Proc. 25th Chin. Control Decis. Conf. (CCDC)*, May 2013, pp. 3243–3247.

[33] P. Aggarwal, Z. Syed, X. Niu, and N. El-Sheimy, "A standard testing and calibration procedure for low cost MEMS inertial sensors and units," *J. Navigat.*, vol. 61, no. 2, pp. 323–336, Apr. 2008.

Javier Martínez Lahoz received the B.Sc. degrees in mechatronics engineering and management engineering from Escuela Universitaria Politécnica de la Almunia (EUPLA), Zaragoza, Spain, in 2016 and 2020, respectively, and the M.Sc. degree in mechatronics engineering from the University of Málaga, Málaga, Spain, in 2019. He is currently pursuing the Ph.D. degree in electronic engineering with the University of Zaragoza, Zaragoza.

He is currently an Associate Professor of electronics with the Escuela Politécnica de la Almunia, University of Zaragoza. His current research interests lie in the design, programming, and optimization of mechatronic systems.

Mr. Martínez Lahoz is a member of the Research Group in Advanced Interfaces (Affective Laboratory), Aragón Institute for Engineering Research, University of Zaragoza.

David Asiaín Ansorena received the B.Sc. degree in electronic engineering from the University of Zaragoza, Zaragoza, Spain, in 2009, and the Ph.D. degree in electronic engineering from Alfonso X el Sabio, Toledo, Spain, 2017.

He is currently an Associate Professor of electronics with the Escuela Politécnica de la Almunia, University of Zaragoza. His current research interests include wearable sensors, wireless sensor networks, the Internet of Things, microelectromechanical system (MEMS) inertial measuring units, and intelligent instrumentation.

Dr. Asiaín Ansorena is a member of the Research Group on Advanced Interfaces (Affective Laboratory), Aragon Institute of Engineering Research, University of Zaragoza.

José Ramón Beltrán Blázquez received the B.Sc. and Ph.D. degrees in physics from the University of Zaragoza, Zaragoza, Spain, in 1988 and 1994, respectively.

He is currently an Associate Professor with the Department of Electronic Engineering and Communications, University of Zaragoza. In 2008, he was a Promoter and Founder of an academic spin-off ARSTIC Audiovisual Solutions S.L., which is devoted to the use of technologies for the artistic and audiovisual fields. He is involved in different research and development projects on audio analysis and processing. His research interests include automatic learning systems for the analysis, processing, and synthesis of musical signals.

Dr. Beltrán Blázquez is a member of the Research Group in Advanced Interfaces (Affective Laboratory), Aragón Institute for Engineering Research, University of Zaragoza.